

# The Induced Mw 5.0 March 2020 West Texas Seismic Sequence

Robert J. Skoumal<sup>1</sup>, J. Ole Kaven<sup>1</sup>, Andrew J. Barbour<sup>1</sup>, Charles Wicks<sup>1</sup>, Michael R. Brudzinski<sup>2</sup>, Elizabeth S. Cochran<sup>1</sup>, Justin L. Rubinstein<sup>1</sup>

<sup>1</sup>U.S. Geological Survey, 350 N. Akron Rd., Moffett Field, California 94035

<sup>2</sup>Department of Geology and Environmental Earth Science, Miami University, 118 Shideler Hall, 250 S. Patterson Ave., Oxford, Ohio 45056

Corresponding author: Robert J. Skoumal (rskoumal@usgs.gov)

# **Key Points:**

- The 25 March 2020 M 5.0 earthquake in West Texas and the seismicity leading up to it was most likely induced by wastewater disposal
- Geodetic slip inversion using InSAR data suggests the mainshock rupture was concentrated above 6 km depth
- Forecasts suggest seismicity rates will likely continue to increase if industry operations are unaltered

This draft manuscript is distributed solely for purposes of scientific peer review. Its content is deliberative and predecisional, so it must not be disclosed or released by reviewers. Because the manuscript has not yet been approved for publication by the U.S. Geological Survey (USGS), it does not represent any official USGS finding or policy.

This article has been accepted for publication and undergone full peer review but has not been through the copyediting, typesetting, pagination and proofreading process, which may lead to differences between this version and the Version of Record. Please cite this article as doi: 10.1029/2020JB020693.

### **Abstract**

On 26 March 2020, a M 5.0 earthquake occurred in the Delaware Basin, Texas, near the border between Reeves and Culberson Counties. This was the third largest earthquake recorded in Texas and the largest earthquake in the Central and Eastern United States since the three M 5.0-5.8 induced events in Oklahoma during 2016. Using multi-station waveform template matching, we detect 3,940 earthquakes in the sequence with the first event in the area occurring in May 2018. The M 5.0 earthquake sequence occurred on a ENE (~082°) normal fault dipping ~37° towards the south. The earthquake caused 6 mm of oblique surface deformation, and geodetic slip inversion suggests slip was isolated above 6 km depth. We find that the sequence was most likely induced by nearby wastewater disposal operations, and seismicity rates in the region surrounding the M 5.0 will likely continue to increase in the future if disposal operations continue unaltered.

### 1. Introduction

Dating back to at least the 1920s, earthquakes have been associated with human activities in Texas (Frohlich et al., 2016). Documented cases of induced seismicity in Texas include earthquakes associated with hydrocarbon production (e.g., Pennington et al., 1986), waterflooding (e.g., Davis & Pennington, 1989), injection of supercritical CO<sub>2</sub> (e.g., Gan & Frohlich, 2013), wastewater disposal (WD) (e.g., Hornbach et al., 2015), and hydraulic fracturing (HF) (e.g., Fasola et al., 2019). The Permian Basin, located in western Texas and southeastern New Mexico, is the largest petroleum-producing basin in the United States. Much of this production has occurred within the Delaware Basin, a sub-basin in the western portion of the Permian Basin. The seismicity rate in the southern Delaware Basin increased by orders of magnitude over the past decade as a result of both increases and changes in industry operations (Frohlich et al., 2019; Skoumal et al., 2020). The majority of this seismicity is most likely due to WD with a lesser contribution due to HF (Skoumal et al., 2020). On the basis of these findings, Skoumal et al. (2020) concluded that both the seismicity rate and number of M > 3 earthquakes would likely continue to increase if the industrial operations in the Delaware Basin were to continue unaltered.

At 15:16:27 on 26 March 2020 (UTC), a M 5.0 earthquake occurred in the Delaware Basin, ~60 km northwest of the city of Pecos (Figure 1a). In the three months preceding the M 5.0 event, the National Earthquake Information Center (NEIC) identified four M > 3 earthquakes within ~3 km of the M 5 epicenter, including a M 3.8 ~6 hours before the mainshock. The 26 March 2020 M 5.0 event is the third largest earthquake recorded in Texas. The two larger earthquakes recorded in Texas, the 1931 MLg 5.8 and 1995 M 5.7 events, were both tectonic, naturally occurring earthquakes (Frohlich & Davis, 2002). Based on felt reports, three M ~5.0-5.5 earthquakes have been suggested to have occurred in the Texas Panhandle in 1925, 1936, and 1948, although there is insufficient evidence to conclude if any of them were probably associated with hydrocarbon production (Frohlich & Davis, 2002). Only four  $M \ge 5.0$  earthquakes have been previously associated with fluid injection activities in the Central and Eastern United States, all of which occurred in Oklahoma (e.g., Keranen et al., 2013; McNamara et al., 2015; Yeck et al., 2016, 2017). If the West Texas M 5.0 was induced by fluid injection activities, it would be among the largest injection induced earthquakes in the world (e.g., Keranen & Weingarten, 2018).

The location of the 26 March 2020 **M** 5.0 earthquake is near seismicity that had previously been found to be induced by wastewater disposal (Skoumal et al., 2020) (Figure 2a).

Additionally, disposal wells in this area induced earthquakes from more than 25 km away to the west due to far-field effects (Skoumal et al., 2020). For the past several years, there have been wastewater disposal, hydraulic fracturing, and hydrocarbon production within 10 km of the **M** 5.0 epicenter.

This study principally seeks to better characterize the 26 March 2020 M 5.0 sequence, identify the cause of the earthquakes, constrain surface displacement using interferogram-based slip model, and to forecast seismicity in the area using physics-based models.

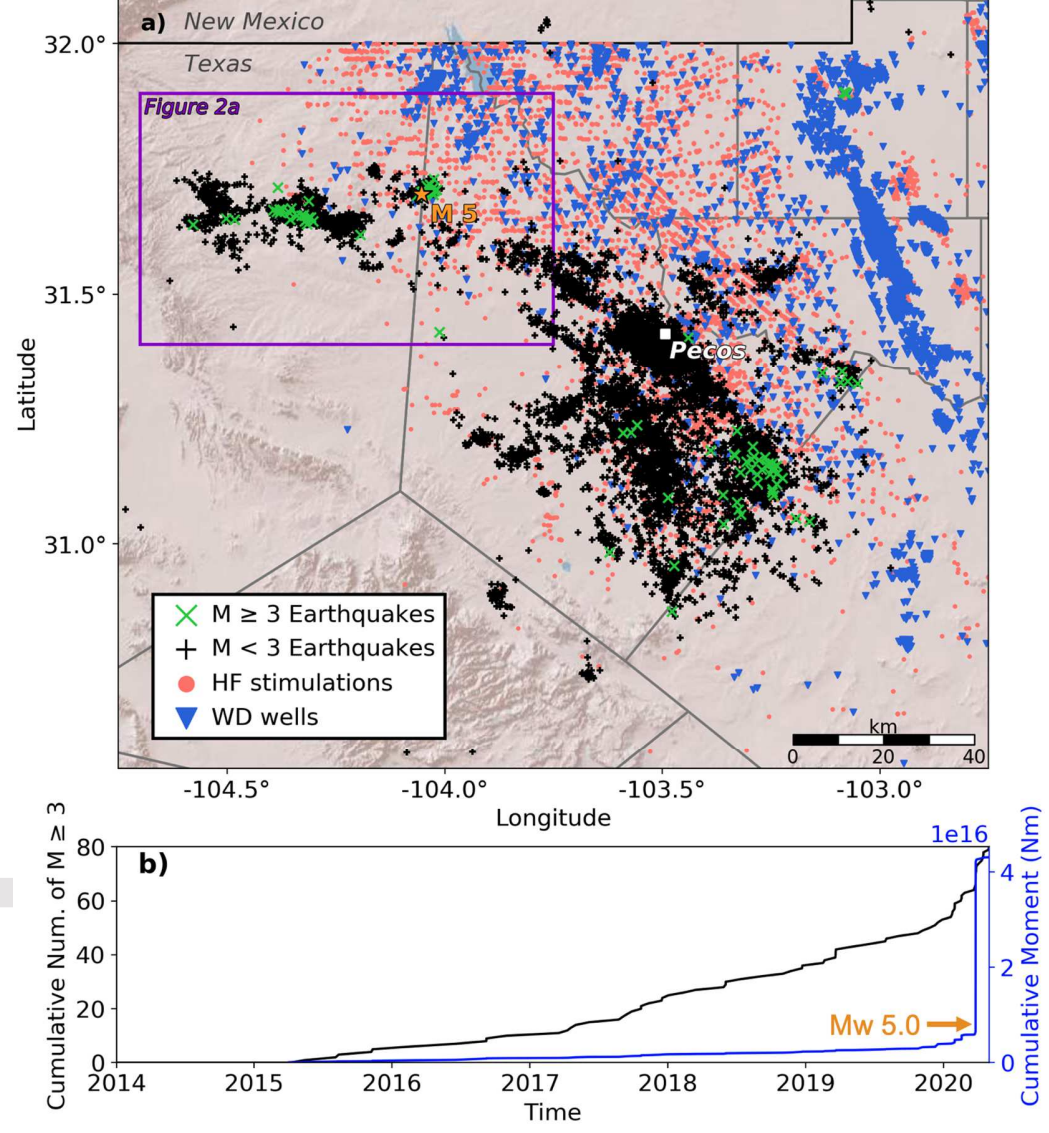


**Figure 1**. a) Map of western Texas showing seismicity and industry operations during 2014-2020 showing the location of the 2020 **M** 5.0 mainshock (star). b) Cumulative number of  $M \ge 3$  earthquakes and their corresponding cumulative seismic moment for seismicity shown in a).

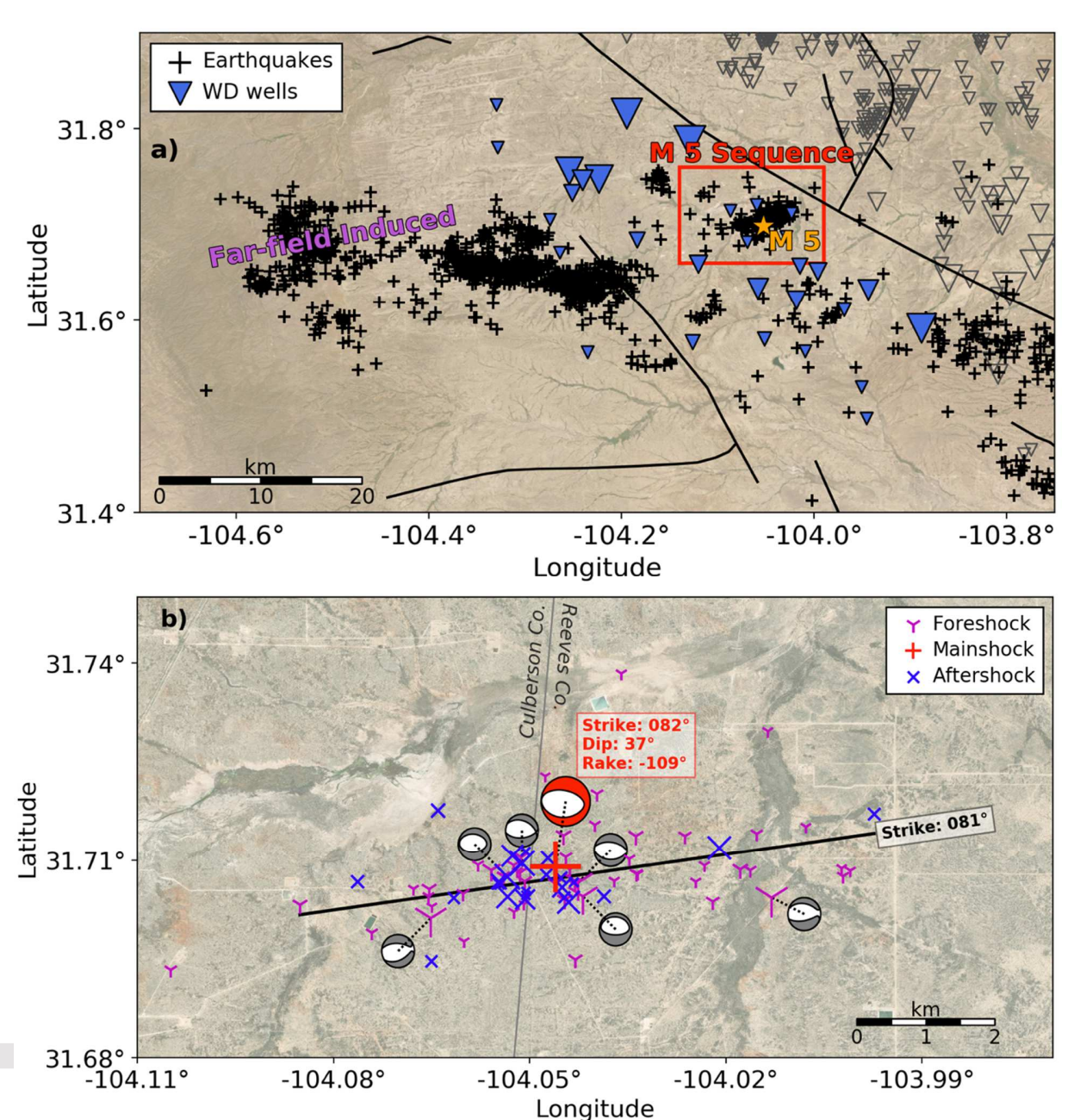


**Figure 2.** a) All seismicity reported in the ComCat and TexNet catalogs are represented by crosses. WD wells are represented by triangles, with filled triangles indicating the wells used in rate-state seismicity modeling. Lines indicate previously mapped faults (Ruppel et al., 2008). All earthquakes within the rectangle were used in the template matching routine. The earthquakes in the western portion of the map were previously found to have been induced by far-field (>25 km) effects from WD wells that may have also induced the **M** 5.0 earthquake (star). b) All of our relative relocations of the **M** 5.0 template matched catalog and moment tensors from the NEIC catalog. The line represents the trend of the sequence determined from our application of FaultID to the epicenter locations.

# 2. Methods

## 2.1 Earthquake Detection

All seismicity in the ANSS Comprehensive Earthquake Catalog (ComCat) and Texas Bureau of Economic Geology TexNet earthquake catalogs in a ~150 km² area around the M 5.0 earthquake (Figure 2a) is used in a multi-station waveform template matching routine. Two template matching approaches are considered using different networks. The first approach uses newer, local stations to characterize seismicity since 2017. The second uses a longer-running array that is located farther from the seismicity, but allows earthquakes to be characterized since 2000.

To characterize recent seismicity, template matching is performed using stations US.MNTX, TX.PECS, and TX.VHRN (hereafter, the "MPV stations") between 28 March 2017 and 1 May 2020. Template waveforms begin 5 s prior to their respective P-wave arrival time and are 30 s in length. Data are filtered between 5-15 Hz in the same manner as previous template matching work in the Delaware Basin (Skoumal et al., 2020).

To characterize seismicity prior to March 2017, a second template matching approach is also performed using the nine single-component seismometers in the TXAR array between 28 April 2000 and 1 May 2020. The TXAR array is located in Lajitas, Texas, near the Texas-Mexico border. Although the array is relatively far (~260 km) from the seismicity of interest, the array is extraordinarily sensitive and was previously used to identify seismicity throughout the Permian Basin with F-K analysis (Frohlich et al., 2019). The TXAR template waveforms begin 5 s prior to their respective P-wave arrival time and are 60 s in length. As the TXAR array has a lower sampling rate of 20 samples/s, data are filtered between 2-10 Hz in the same manner as Frohlich et al. (2019).

In both template matching approaches, successful detections are defined as matches that exceed 15 times the daily median absolute deviation (MAD) of the network normalized cross-correlation coefficients, a previously demonstrated conservative threshold (e.g., Skoumal et al., 2014).

For newly identified earthquakes, we estimate their magnitudes by comparing the unnormalized correlation coefficient between the new event and their respective template earthquake following the approach of Schaff & Richards (2014). This magnitude estimate is defined as:

$$\delta_{mag} = log_{10}[max(\mathbf{x} \star \mathbf{y})/(\mathbf{x} \cdot \mathbf{x})] \quad (1)$$

where  $\star$  represents cross-correlation, centered dot (·) is the dot product, and x and y represent the waveforms of the template and detected earthquake, respectively. For a given event, we calculate the median  $\delta_{mag}$  value for all channels that are used to detect it. For template earthquakes identified by both the NEIC and TexNet, we give preference to magnitudes reported by the NEIC.

## 2.2 Earthquake Relocation

As TexNet does not publicly disclose their phase picks, we manually re-identify phase arrivals for the 130 earthquakes in TexNet catalog within our study area (Figure 2a). Absolute earthquake locations are determined using NonLinLoc (Lomax et al., 2000) with a 1-D velocity model previously developed by Savvaidis et al. (2019) for the Delaware Basin (Table S1). We assumed that uncertainties in *a priori* information (e.g., phase arrival pick times and theoretical

arrival times) are Gaussian and independent of one another, which permits calculation of the posterior probability density function (PDF) for hypocenter parameters using the OctTree sampling algorithm (Husen and Smith, 2004). Using the station residuals produced by NonLinLoc, the location routine is repeated a second time with weighting the stations by those residuals to produce absolute locations.

We propagate our manual phase picks through our template-matched catalog by cross-correlating a 5 sec window encompassing each manual phase pick with the matched waveforms. If the normalized cross-correlation coefficient exceeds 0.7, an "automated" phase pick time is assigned to the newly detected event. Using the manual and automated phase picks, the phase arrivals are correlated against the template-matched catalog to produce differential times and cross-correlation coefficients. Relative earthquake locations are determined using GrowClust (Trugman and Shearer, 2017) using the lag and correlation coefficients between event pairs. For the cluster merging in GrowClust, we define a maximum station distance of 100 km and a maximum root mean square (rms) differential time residual of 0.2 s. GrowClust's nonparametric uncertainty estimation algorithm is used to determine location uncertainty by considering 100 bootstrap iterations.

Using our relocated earthquake catalog, we attempt to estimate the primary fault orientation of the M 5.0 sequence. To determine the fault plane in a quantitative, reproducible, and rapid manner, we applied the FaultID algorithm (Skoumal et al., 2019; Cochran et al., 2020). The FaultID algorithm iteratively spatially clusters earthquakes. Within each cluster, models that represent possible trace(s)/plane(s) to describe the seismicity are evaluated. The output of FaultID consists of the location and orientation for each seismogenic fault. Here, we treat our relocated earthquake catalog as a single spatial cluster as input to FaultID. As the earthquake depths are poorly constrained (see Section 3.1 Improved Earthquake Catalog), we end up fitting the seismicity to a vertical plane. We compare the optimal model with the moment tensors reported by the NEIC to validate the orientation of the fault, and this fault is then used as the basis for our geodetic slip inversion.

## 2.3 Geodetic slip inversion using InSAR data

Coseismic surface deformation can elucidate slip distributions and place further bounds on the nucleation depths of earthquakes independently of the hypocentral locations derived from seismic data. If significant surface displacements are observed, inverting for slip may aid our understanding of the **M** 5 earthquake.

Measurements of surface displacement come from interfering European Space Agency Sentinel 1 satellite synthetic aperture radar (SAR) data. We process Sentinel SAR images into differential interferograms using the SRTM DEM (Farr et al., 2007) to remove topographic phase. We then filter the interferograms, unwrap them, and convert them to line-of-sight (LOS) displacement using standard procesing pratices. To increase the signal-to-noise ratio, we stack 10 interferograms (Table S2, S3) spanning the time of the earthquake: five in an ascending satellite path and five in a descending satellite path. We reduce the number of data points using the quadtree windowing method (Jónsson et al., 2002) and a model-based windowing scheme (Lohman & Simons, 2005; Wicks et al., 2013). The model-based resampling requires two iterations. First, we construct a forward model of the deformation fields to calculate quadtree windows for resampling the observed data. After inversion for a deformation source using these windowed data, we then calculate new quadtree windows using the model found through

inversion. The observed LOS interferograms are then resampled again, and the final model is fit to these data.

The reduced stacked interferograms are used to invert for slip on a single, planar fault surface that is constrained by our FaultID results and the NEIC moment tensor solution (described in Section 3.1 Improved Earthquake Catalog) for the mainshock (strike 082° and dip 37°) (Figure 2b). While we assign the fault geometry, we do not impose any hypocentral depth and allow slip to freely vary along the prescribed surface. We constrain the geodetic slip inversion model solutions by prescribing that all slip on the fault is in the dip-slip direction (normal faulting sense) and that no strike-slip nor opening can take place. The inversion for dipslip only is carried out as we seek to understand whether a simple slip model can offer independent verification of the hypocentral depth and the subsequent slip. We do not constrain the total geodetic moment and we do not impose any specific hypocentral depth in the solution. We solve the resulting inverse problem using a nonnegative least squares solver (Murray and Langbein, 2006). We use standard geodetic inversion methods by solving a non-negative least squares problem while applying spatial Laplace smoothing on the triangular mesh (Murray and Langbein, 2006). We select the smoothing parameter  $(\gamma)$  based on the reduction in data and model misfits by cross-validating  $\gamma$  (Wahba, 1990) (Figure S1). For each value of  $\gamma$  we estimate the residuals at the randomly omitted data points and sum those for all observations to arrive at the cross validation of sum of squares (CVSS).

# 2.4 Induced seismicity rate modeling

We use numerical modeling to better understand the proposed connection between wastewater disposal and the observed rates of induced seismicity, and to forecast future seismicity rates. Fluid pressure changes due to injection are an important factor controlling induced seismicity by bringing faults closer to failure (e.g., Shapiro & Dinske, 2009), but earthquake rates that lag injection rates could also be explained by transient earthquake nucleation effects (Dieterich, 1994; Segall and Lu, 2015). With rate-and-state dependent friction, earthquake rates are related to (1) the preexisting state of stress and pore fluid pressure acting on the faults, (2) changes in the rate of Coulomb failure stresses felt by the faults, and (3) the frictional response of the rock. The non-linear relationship between stressing rates and seismicity rates offers a mechanism for the differences between the histories of injection and seismicity seen in the Delaware Basin over multiple timescales.

In neighboring Oklahoma and Kansas, as well as elsewhere in Texas, the Dieterich-type earthquake nucleation model fits the observed injection induced seismicity rates quite well (Norbeck and Rubinstein, 2018; Zhai and Shirzaei, 2018; Zhai, et al., 2019). In Fort Worth, Texas, seismic activity resulting from injection persists long after operations cease (e.g., Ogwari, et al., 2018). To test whether the rate-and-state model holds for our region of interest, we adopt the approach of Norbeck and Rubinstein (2018) to model the seismicity rates from wastewater disposal volumes alone. This approach treats the disposal reservoir as a confined, fluid-saturated porous medium wherein the effects of compressibility of a fluid-saturated medium determine the stress changes at seismogenic depths caused by the addition of injected fluids. While formations like the interbedded shales (e.g., Wolfcamp, Barnett, Woodford) and the basement may inhibit the vertical migration of fluids, treating the reservoir as a confined system is a modeling simplification. The true degree to which vertical flow is restricted is unknown but could be determined with pore pressure measurements that currently do not exist in the public domain. The assumed response of the fluid-rock system is a gross simplification of both the geologic

complexity and the physics relating poroelastic deformation and fluid pressure changes to fluid injection (e.g., Segall and Lu, 2015), but the general approach is supported by studies that utilize physical models of injection in Oklahoma (e.g., Barbour, et al., 2017; Goebel, et al., 2017; Zhai and Shirzaei, 2018; Langenbruch, et al., 2019).

We restrict this analysis to the WD wells shown in Figure 2a. WD occurred beginning in 2013 with volumes generally increasing over time (Figure 3). For eight of the 30 WD wells, we lacked between 1-8 months of the most recent disposal volumes prior to the M 5.0 earthquake (Figure S2). To fill in those gaps, we assume injection rates continue at constant rate equal to the average of the previous six months. As disposal rates have generally increased over the past five years, this likely provides a conservative (i.e. smaller) estimate for the actual injected volumes. The injected volumes at month m,  $\Delta V_m$ , are used to calculate reservoir pressurization rates following Norbeck and Rubinstein (2018):

$$\dot{p}_m = \Delta V_m / (\beta \cdot \phi \cdot V) \tag{2}$$

where V is the closed reservoir volume,  $\beta$  is the sum of fluid and pore compressibility for variable confining pressure, and  $\phi$  is the fraction of the bulk volume V occupied by pore space (porosity). The quantity  $\beta \cdot \phi$  is therefore equivalent to the bulk compressibility under variable pore fluid pressure (Zimmerman, et al., 1986, Equation 2). We assume the reservoir has a uniform thickness and extends across the model domain; thus the pressurization rate is assumed to represent upper bounds on rates of Coulomb failure stress changes at seismogenic depths ( $\dot{s}$ ):

$$\dot{s} \cong \dot{p}_m \tag{3}$$

Following Segall and Lu (2015), the Dieterich (1994) type seismicity response behaves according to the ordinary differential equation:

$$\frac{dR}{dt} = \frac{R}{t_c} \left( \frac{\dot{s}}{\dot{s}_0} - R \right) \tag{4}$$

where  $\dot{s}_0$  is the background stressing rate and  $t_c$  is the characteristic relaxation timescale; the number of earthquakes r is given by  $R \cdot r_0$ , where  $r_0$  is the background seismicity rate. The characteristic timescale  $t_c$  determines the time evolution necessary for  $r \rightarrow r_0$ ; it is also related inversely to the background stressing rate and directly related to the direct effect parameter in the rate-and-state friction equation (A) multiplied by the effective normal stress  $(\sigma)$ :

$$t_c = A\sigma/\dot{s}_0 \qquad (5)$$

We first solve this problem numerically using adaptive time-stepping to obtain a timeseries for R, and then we resample using linear interpolation to get monthly values,  $R_m$ .

This model relating seismicity rate changes to injection volumes is appealing in its simplicity and flexibility: the expression governing the evolution of seismicity rates is agnostic to the mechanism by which  $\dot{s}$  is calculated, and its solution represents seismicity rates in a finite crustal volume. For instance, while Norbeck and Rubinstein (2018) used the simplified reservoir compressibility model adopted here, Zhai and Shirzaei (2018) calculated  $\dot{s}$  from a fully-coupled poroelastic model of injection in a layered halfspace (e.g., Barbour, et al., 2017) based on the method of Wang and Kümpel (2003). Relatively few parameters are needed to solve for R, and all of them are related to physical properties of the subsurface rather than from a statistical calibration. We use previous studies (Table 1) to set the bounds for these parameters, and use non-linear inversion to solve for parameters that minimize the sum of squared residuals between the model and the observed seismicity rates.

To forecast future seismicity, we consider six cases of future injection to inform the optimized seismicity model: (1) constant-rate injection equal to the assumed average rate in the six-months prior to the 2020 M 5 earthquake, (2) a constant reduction in rate by 50% over 5

years, (3) a constant reduction by 75%, (4) a parabolic reduction in rate by 50%, (5) a parabolic reduction in rate by 75%, and (6) a complete shut-in (i.e. no further injection) of all wells. All of these scenarios optimistically involve no further increases in disposal volumes to evaluate the potential efficacy of mitigation actions.

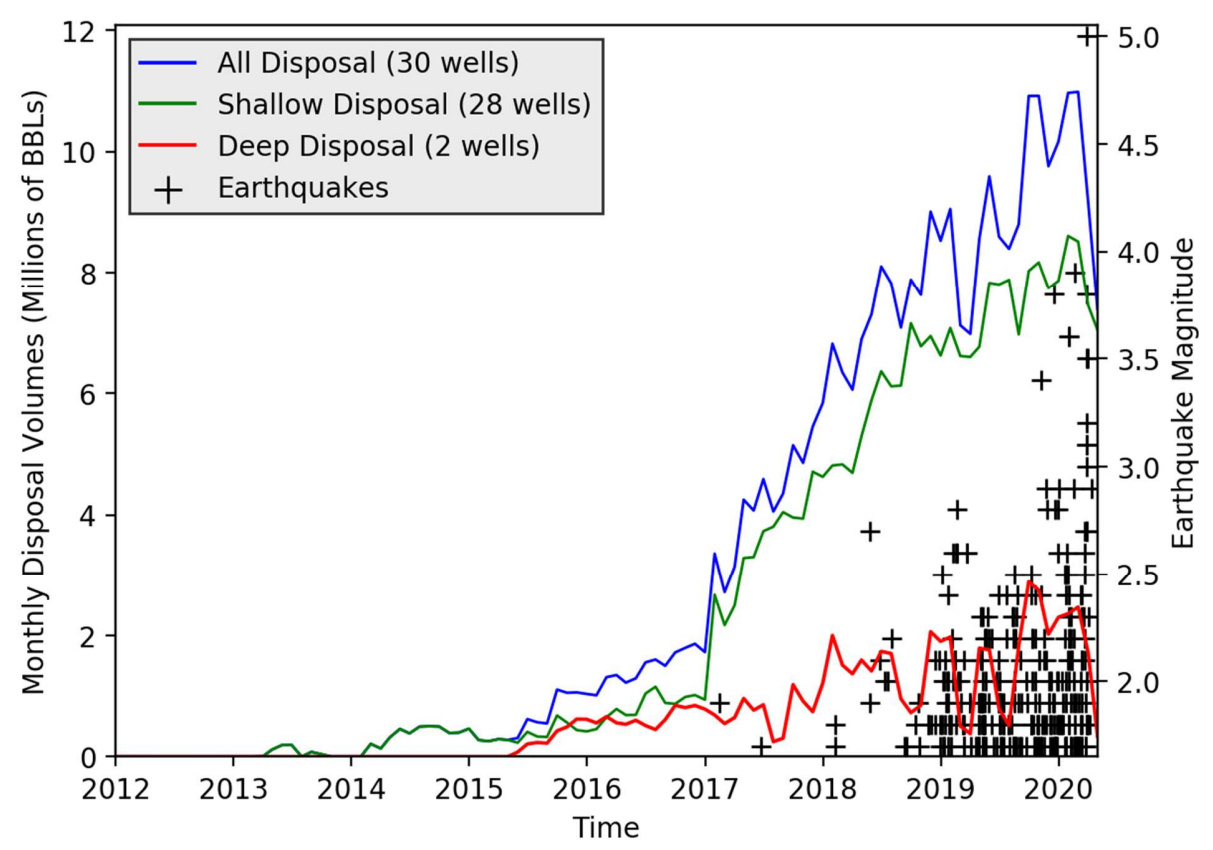


**Figure 3**. Monthly reported wastewater disposal volumes (lines) in the region around the **M** 5 sequence (Figure 2a) compared with earthquake magnitudes (crosses) above the magnitude of completeness.

# 3. Results & Discussion

# 3.1 Improved earthquake catalog

Using the 130 earthquakes from the TexNet and NEIC catalogs as templates, our improved earthquake catalog using the MPV array contains 3,940 earthquakes while the TXAR array located much farther from the sequence away produces a catalog with 785 earthquakes (Figure 4). The results from both template matching applications display nearly identical temporal earthquake patterns with the first earthquake identified in both catalogs on 22 May 2018 (Figure 4b). While template matching is a powerful technique for identifying seismicity similar in character (i.e. similar location and mechanism) to a known earthquake, it cannot efficiently identify events that are dissimilar to previously identified earthquakes. We conclude that there was no notable ( $\mathbf{M} \gtrsim 1$ ) seismicity that closely resembles the earthquakes identified in the  $\mathbf{M}$  5 sequence between April 2000 and May 2018. However, seismic sequences along other

faults in the area that remained below the TexNet magnitude of completeness ( $M_C \approx 1.7$ ) are likely not fully represented in our catalogs.

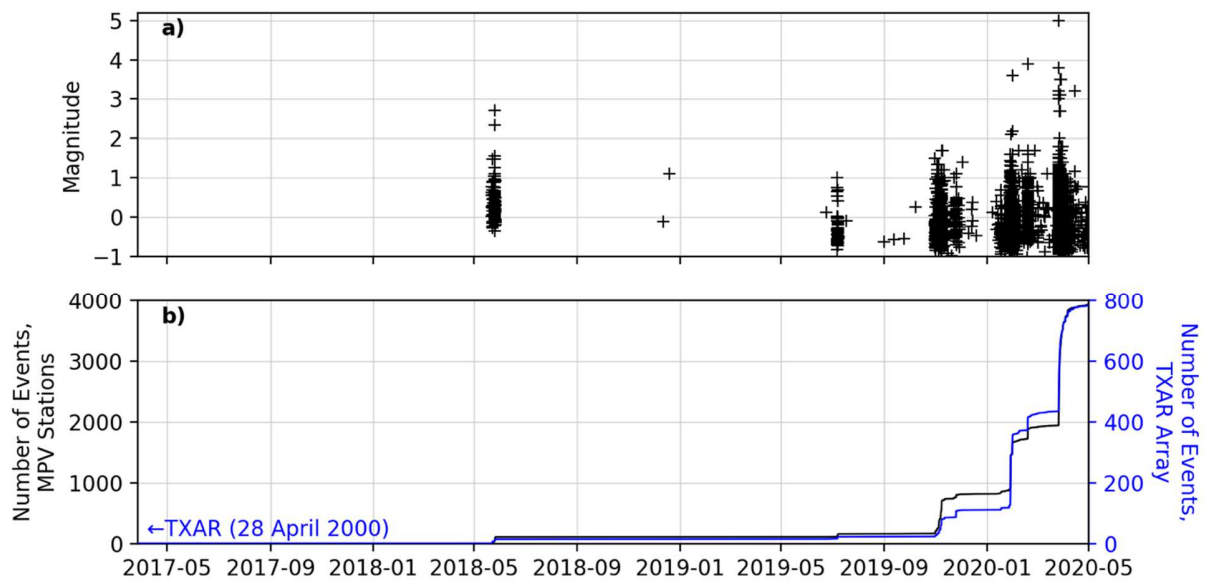


**Figure 4**. a) Magnitudes of earthquakes versus time in our improved catalog. b) Cumulative number of events detected from template matching using the MPV and TXAR arrays. The processing using the TXAR network extends back to 28 April 2000, but no events were found prior to 22 May 2018.

The integrated locations of our relocated earthquake catalog for the M 5 sequence extend across the Reeves and Culberson County border (Figure 2b). As the nearest seismometer is  $\sim\!25$  km from the sequence (much greater than the hypocentral depth), the depths of the relocated earthquakes are poorly constrained with average vertical uncertainties for the sequence of 10.1 ( $\pm 4.2$ ) km (Figure 5). As a result, the dip of the fault plane cannot be resolved by applying FaultID to the earthquake hypocenters. However, by only considering the epicenters of the events as was done in previous work (Skoumal et al., 2019), the fault trend can still be identified. The resulting trend suggests an ENE fault with an azimuth of N81°E. This is in good agreement with the strike of the nearby moment tensors, and allows us to confidently characterize the correct nodal plane with an approximate strike: 082°, dip: 37°, and rake: -109°.

The horizontal uncertainty from our analysis is similar to NEIC's (2.4 and 2.5 km, respectively). Constraining the depth of the M 5 mainshock is important for our understanding of the sequence, but the NonLinLoc results suggest that the earthquake can be explained by a wide range of depths of  $8.7 \, (\pm 6.4) \, \text{km}$ . As the nearest seismometer is more than a focal depth away from the event, TexNet's reported depth uncertainty of  $1.9 \, \text{km}$  is likely underestimated. Despite the complex geology and velocity structure in the Permian Basin, our use of a simple one-dimensional velocity model (Table S1) severely limits the accuracy of hypocentral parameters. The three-dimensional velocity model for the Delaware Basin in development (Rathje et al., 2018) was unavailable at the time of this writing; however, such a model could be used to provide greater insight into the hypocentral locations of the events when it becomes available.

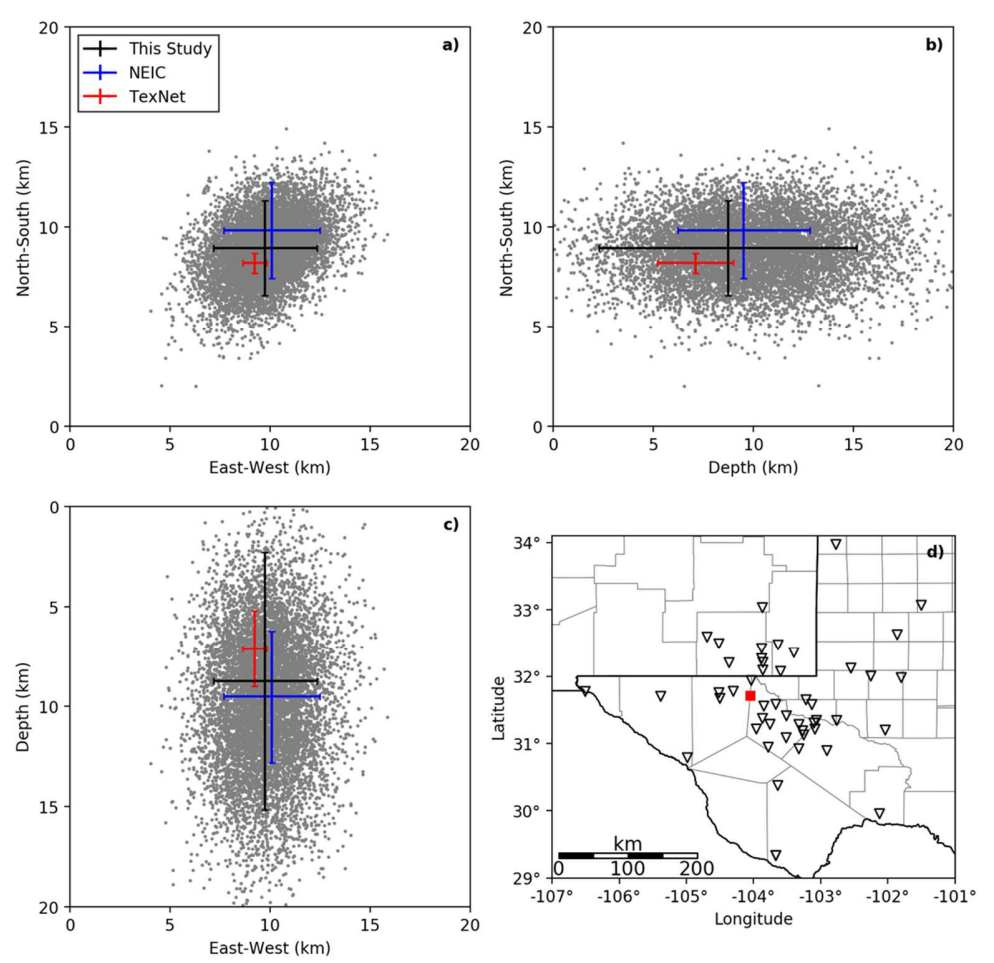


**Figure 5**. Differences in the reported location of the 2020 **M** 5.0 hypocenter. a-c) Hypocentral location uncertainties (lines) and covariate scatter clouds (dots) of the **M** 5.0 determined in our study using NonLinLoc compared with locations reported by the NEIC and TexNet. Note that the TexNet uncertainties may be underreported. d) Seismometers utilized in our location of the **M** 5.0 are shown as triangles. The region represented in a) is shown as a filled rectangle.

# 3.2 Geodetic slip inversion

The stacked interferograms reveal maximum LOS surface displacement of 6 mm centered around the epicenter. Uncertainties in the LOS surface displacement for the descending path are as high as 1.5 mm in the epicentral region (Figure S3). Given the relatively large uncertainties in hypocentral location estimated from our relocated catalog, we use the geodetic slip inversion to further constrain the depth of the **M** 5.0 earthquake. Our slip model shows smoothly varying slip over an area about 14 km along strike and 6-8 km down dip to a depth of ~6 km (Figure 6). The maximum slip is ~1.2 cm and the total geodetic moment is  $1.71 \times 10^{16}$  Nm, which is equivalent to **M** 4.8. The resulting slip distribution suggests that the coseismic surface displacement is related to shallow slip, extending from about 2 km to 6 km depth. Geodetic slip inversions using InSAR data have been shown to overestimate source depths (Pederson et al., 2003; Funning et al., 2005), which suggests that the hypocentral depth is likely shallower than

the maximum likelihood estimate of hypocentral depth (8.7 km) from our analyses, but still within our uncertainty estimate.

Generally, a M 5 with normal mechanism at crustal depths greater than 6 km is unlikely to generate observable surface deformation. As the observed oblique surface displacement is as large as 6 mm and well outside of the noise, this finding supports a relatively shallow (< 6 km) hypocenter. This finding aids our understanding of the M 5 and the factors that lead to its occurrence (described in *Section 3.4 Cause of the M 5.0 Sequence*)

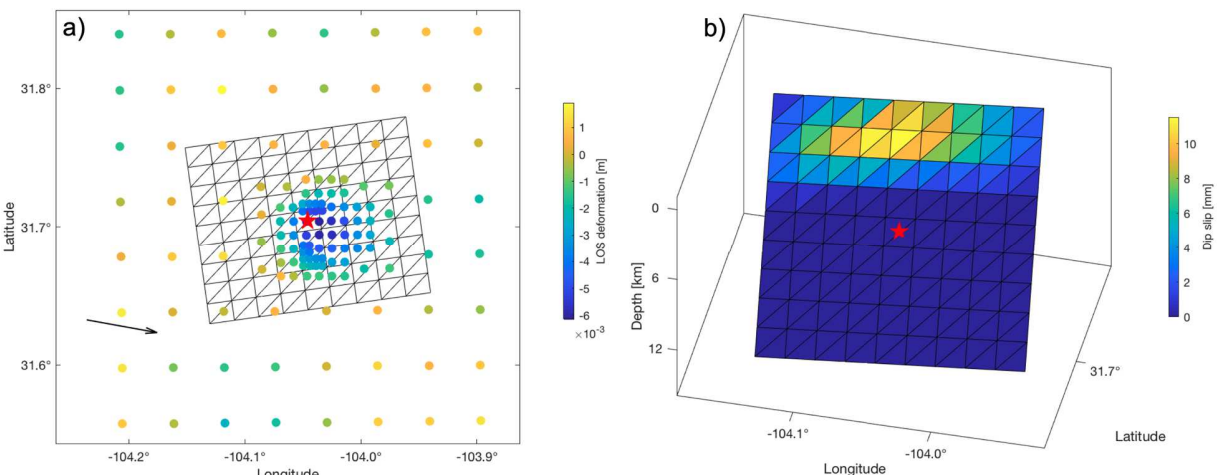


**Figure 6**. Ground deformation and kinematics of the 2020 M5 event. a) Line-of-Sight (LOS) displacements from stacked interferograms after a quadtree decomposition on irregular spatial tiles shown by filled circles at each tiles' centroid. The arrow indicates the LOS direction. The **M** 5.0 epicenter is represented as a star. b) Resulting slip distribution is on a planar fault striking 082° and dipping 37°. Hypocenter of the **M** 5.0 earthquake is shown as a star.

## 3.3 Induced seismicity rate modeling

Our observational and slip inversion analyses suggest WD likely induced slip within the sedimentary strata (see Section 3.4 Cause of the M 5.0 Sequence). With this understanding, we seek to investigate how the nearby WD well operations related to the observed increase in seismicity. Additionally, we consider how operational decisions at these WD wells might influence future earthquake occurrence by modeling the influence that disposal wells have on seismicity rate in the area around the M 5.0 sequence.

Like with any model, the rate-state seismicity results are subject to uncertainties in the input parameters. We run sensitivity results to test a broad spectrum of seismicity responses (Table S2). At low  $A\sigma$  ( $\lesssim$ 0.1 MPa), the response more closely resembles the injection history, with the seismicity rates primarily controlled by the background stressing rate. At higher values of  $A\sigma$ , the response is smoother and does not share much resemblance with the injection timeseries. Increasing the bulk compressibility  $\phi\beta$  decreases the Coulomb stressing rates and effectively minimizes the seismicity response, especially when background stressing rates are low.

In order to make more quantitative interpretations for this region, we use sensitivity tests and prior studies to choose both a starting model and upper and lower bounds for a non-linear least-squares optimization using a box-constrained, quasi-Newton method (Byrd, et al., 1995).

From this optimization we obtain the background stressing rate ( $\dot{s}_0$ ), background seismicity rate ( $\dot{r}_0$ ), bulk compressibility ( $\beta\phi$ ), and a rate-and-state parameter ( $A\sigma$ ); since the parameters A and  $\sigma$ , as well as  $\phi$  and  $\beta$ , are inseparable (see Equations 2 and 5), we fix  $\beta$  to estimate  $\phi$ , and use both laboratory-derived relationships (Blanpied, et al., 1998) and inferred gradients of effective normal stress in Texas (Lund-Snee and Zoback, 2016) to estimate A.

The optimized inverse solution shows very good agreement with the observed increase in seismicity over time (Figure 7). The specific coefficients we obtain are tabulated in Table 1. The observed earthquake rate can be matched using a background earthquake rate of roughly 1  $M \ge M_C$  event every 31 years and a background stressing rate of 23 kPa/yr; together these suggest a regional strain rate between the values measured by Anderson (1986) and Calais, et al (2006), around  $10^{-10}$  yr<sup>-1</sup> (see Supplemental Material). The optimal value of  $\phi\beta$  is  $6.3\times10^{-10}$  Pa<sup>-1</sup>, which means that if the fluid bulk modulus is 2.3 GPa (e.g., water), and the solid bulk modulus is between 10 and 30 GPa (e.g., between sandstone and granite; Wang, 2000, Appendix C), the representative porosity is likely between 0.12 and 0.14; if, however, the fluid bulk modulus is 3.3 GPa (e.g., water at high confining pressure), the porosity is likely between 0.16 and 0.19.

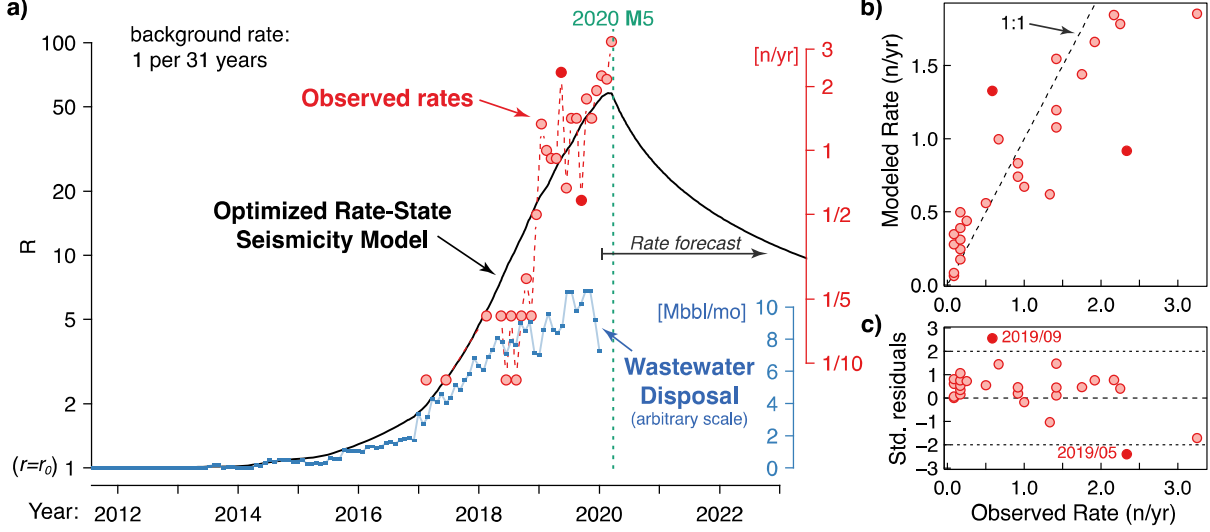


**Figure 7**. Rate-and-state seismicity model based on wastewater disposal volumes in proximity to the 2020 **M** 5.0 earthquake (Figures 2 and 3). (a) Modeled seismicity rate changes ( $R = r/r_0$ ; Equation 4) compared to observed annual seismicity rates ( $M \ge M_C$ ), on logarithmic scales, with disposal volumes. After the last reported disposal volume, the model represents a forecast assuming injection operations cease (i.e. shut-in). (b) Scatter plot of modeled rate, based on the value of R multiplied by  $r_0$ , the best-fitting background rate from the optimization (1 event every 31 years), as a function of observed rate. (c) Model residuals that have been normalized to unit variance (standardized): May and September of 2019 (filled circles in (a)) are the months with the highest and lowest observed rates of earthquakes compared to the rate-and-state seismicity model, respectively.

The optimal value of  $A\sigma$  is 0.83 MPa. Lund-Snee and Zoback (2016) used their estimates of the state of stress in Texas to identify the plausible range of stresses and pore pressures for some recent earthquakes in Snyder, Texas (1978 M 4.5, 2011 M 4.4), and Timpson, Texas (2012 M 4.8, 2012 M 3.8). For reference, the earthquakes in Snyder, near the Cogdell oil field, are the

closest events to our study region. Lund-Snee and Zoback (2016) reported the effective normal stress gradients in the case of high and low (hydrostatic) pore pressure, which are reported to be 7 and 11 MPa/km for Snyder, and 5 and 14 MPa/km for Timpson, respectively. At the mean earthquake nucleation depth (7.3 km; Figure 8), these gradients give a range of effective normal stress for the region ( $\sigma^{TX}$ ) of 51 to 80 MPa, and 37 and 102 MPa, respectively; thus, the range of  $A\sigma/\sigma^{TX}$  is 0.010 to 0.016, and 0.0081 to 0.023, respectively. Lockner (1998) reported that Westerley granite at room temperature shows behavior consistent with A = 0.008 over a wide range of confining pressures, but Blanpied, et al. (1998) showed that under hydrothermal conditions the parameter A shows a temperature dependence, with A(T) = 0.02127 - 3/T for T < 543°K (270°C) and A(T) = 0.17838 - 88.14/T for  $T \ge 543$ °K. We tested three representative geothermal gradients for the Permian Basin from Ruppel et al. (2005), namely a low estimate of 22°C/km (low), the most commonly estimated 25°C/km, and a high estimate 29°C/km, finding that earthquake nucleation depths are largely consistent with the T < 270°C frictional regime. Furthermore, the value of A at mean earthquake depths is tightly constrained to be  $\sim 0.015$ (Figure 8), differences in rock type notwithstanding. Hence, while A plausibly varies between 0.0081 and 0.023, we assume it is in closer agreement with the hydrothermal estimate; in that case the effective normal stress is 55 MPa for an average gradient of ~7.5 MPa/km.

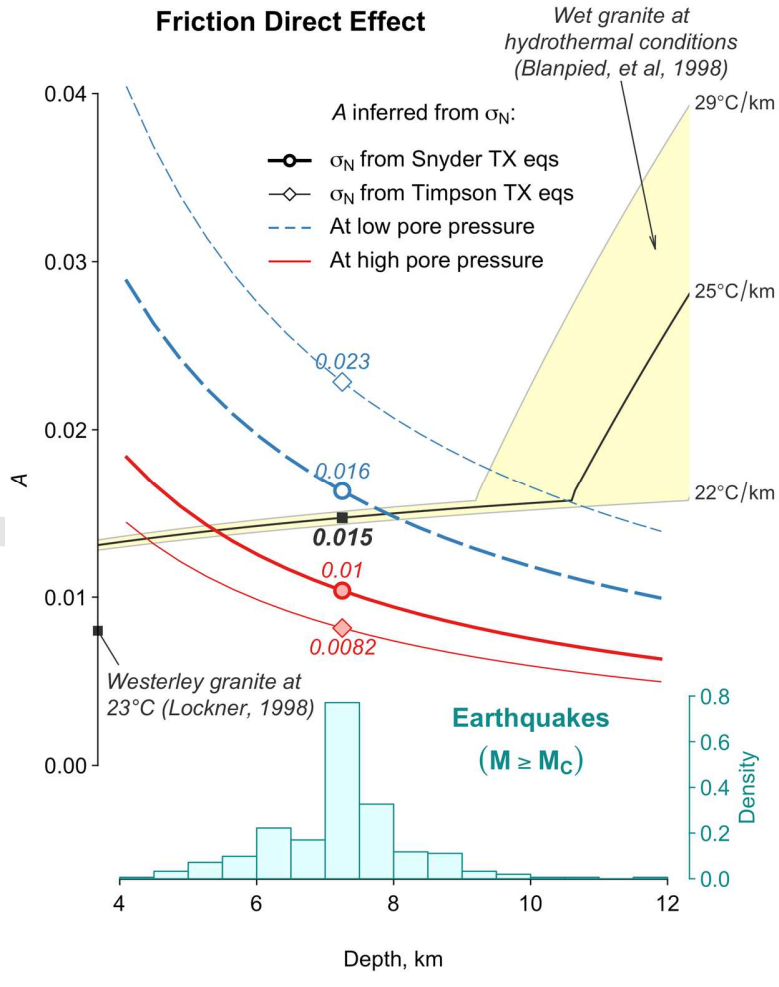


**Figure 8**. Estimates of the friction direct effect parameter A with depth from local stress gradients and rock constitutive relationships. Thick and thin lines show the value of  $A\sigma$  from our optimized seismicity rate model scaled by the effective normal stress gradients inferred from earthquakes in Snyder and Timpson, Texas, respectively (from Lund-Snee and Zoback, 2016); red and blue lines show the results for gradients based on scenarios of high and low pore pressure at fault reactivation. The filled region is based on the hydrothermal response of wet granite (Blanpied, et al., 1998) at three characteristic geothermal temperature gradients for the Permian Basin (Ruppel et al., 2005). The point on the left, at 0.008, is representative of granite at room temperature (Lockner, 1998). The histogram on the bottom shows the density of earthquake depths in this region, and the circles and squares show estimates at the mean earthquake depth.

Using the same model and parameters, we can look forward in time to forecast seismicity for six injection volume reduction scenarios. The forecast results (Figure 9) suggest that the earthquake rates would reduce in cases where total wastewater disposal rates are reduced by more than 50% of their present rate. The parabolic reductions in rate (scaling as  $1/t^2$ ) are more effective at reducing seismicity rates at early times, but over very long times they approach the results for the linear reductions (scaling as 1/t). This is because both scenarios reach the same total injection rate and the seismicity rate reaches a steady-state that is proportional to the stressing rate. Both linear reduction scenarios and the weaker parabolic reduction scenario cause transient increases in seismicity rate before they reduce (e.g., Segall and Lu, 2015), because they represent relatively strong departures from the manner in which reported disposal rates were changing prior to the M 5 earthquake. The generally sluggish reduction in seismicity rates, even for the vigorous reduction scenarios, is primarily a consequence of the background stressing rate  $\dot{s}_0$  being much smaller than the rate-and-state parameter  $A\sigma$ , and thus the characteristic relaxation time (Equation 5) becomes very long.

Our future-injection scenarios do not consider the transient effect of poroelastic coupling that may influence rates considerably, especially in certain faulting regimes (i.e., Segall and Lu, 2015; Fan et al., 2019). A key parameter that determines the strength of coupling is the value of Biot's effective stress coefficient ( $\alpha$ ) in the rock layers. According to Zimmerman, et al., (1986), a lower bound for  $\alpha$  is given by the porosity and the Poisson's ratio ( $\nu$ ):

$$\alpha = \frac{1 + \nu + 2\phi(1 - 2\nu)}{3(1 - \nu)}$$
 (6)

Based on the optimized porosity estimate,  $\alpha$  must be greater than 0.41 (for the improbable case where  $\nu=0$ ), but is more likely between 0.61 and 0.80 for  $\nu=0.25$  and  $\nu=0.4$ . This is the range generally expected for more compliant and permeable rock types such as sandstone (Wang, 2000). These estimates indicate a strong possibility that poroelastic coupling related to rapid changes (whether increases or decreases) in disposal rate will further influence seismicity rates in the Permian Basin. A poroelastic coupling effect was previously inferred leading up to the 2016 **M** 5.8 Pawnee earthquake, where the seismicity seen prior to the mainshock was related to the change in wastewater disposal rates over a relatively short time period (Barbour et al., 2017). The long decay of induced seismicity rates in the Dallas/Fort Worth area (Ogwari et al., 2018) is an indication that the slow decay times forecasted for this area of the Permian Basin is a plausible outcome that cannot be discounted.

**Table 1**. Optimized seismicity model parameters determined for this study versus those used in other induced seismicity work in Texas, Kansas, and Oklahoma. Parentheses indicate calculated or inferred values.

_			Delaware Basin	North Central Texas	Oklahoma and Southern Kansas	West and Central Oklahoma	Oklahoma (2016 M 5.8 Pawnee)
	Parameter [Units]	Description	Optimal values from this study	Zhai and Shirzaei (2018)	(Norbeck and Rubinstein, 2018)	(Zhai, et al., 2019)	Barbour, et al., 2017)
	β [1/GPa]	Total compressibility	(0.33-0.52)	-	0.32	-	-
	ф	Porosity	(0.12-0.19)	-	0.12	-	-
	β φ [1/GPa]	Bulk compressibility	0.0629		(0.0384)	-	-
	ṡ₀ [kPa/yr]	Background stressing rate	0.0234	0.01	0.7	0.01	0.1
	A	Direct effect parameter	(0.0081-0.023)	0.003	0.0065	0.003	0.003
	σ [MPa]	Effective normal stress	(36-102)	35	50	22	20
	Aσ [MPa]	Rate-and-state parameter	0.828	(0.105)	(0.325)	(0.066)	(0.06)

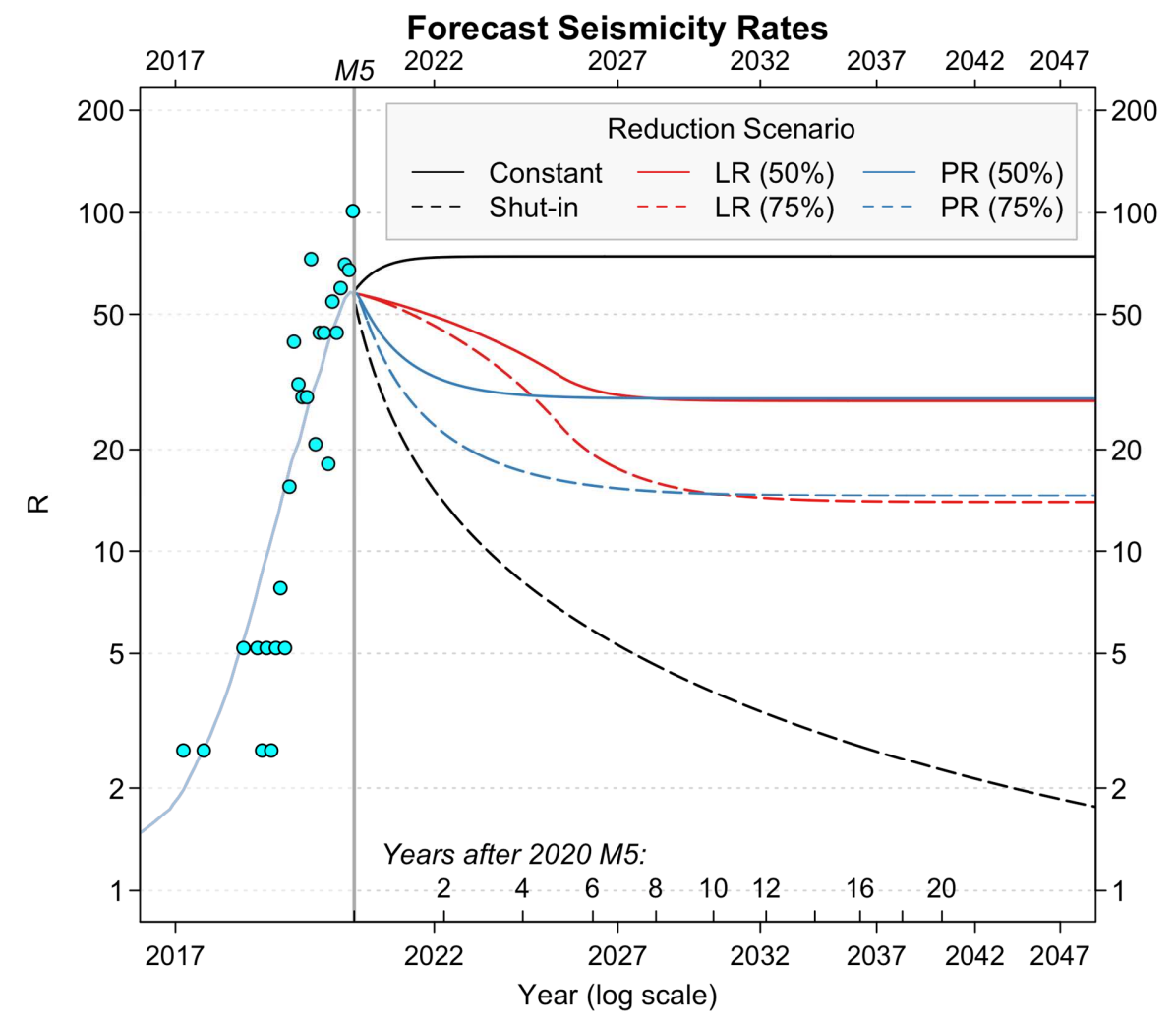


**Figure 9**. Forecasts of increases in seismicity rate ( $R = r/r_0$ ; Equation 4) for ~30 years after the **M** 5.0 earthquake considering various injection volume reduction scenarios. All scales are logarithmic. The optimized rate-and-state seismicity model is shown prior to the **M** 5, as well as the observed earthquake rates scaled by  $r_0$  (circles). After the **M** 5 shows the results of applying the optimized model (Table 1) to six different future-injection scenarios (see Supporting Information). Constant: hold steady at average levels from the past six months. Shut-in: cease all injection completely. LR: linear reduction in rates over time. PR: parabolic reduction in rates over time.

# 3.4 Cause of the M 5.0 Sequence

HF-induced seismic sequences have extremely strong temporal correlations during the periods of stimulation activity (e.g., Skoumal et al., 2018), and seismicity is frequently limited to within a few km from the stimulation stage (e.g., Schultz et al., 2020). The vast majority of earthquakes in the sequence are unlikely to be associated with HF as stimulations were either not occurring or were  $\geq 10$  km from the events. At the time of the M 5.0, no known stimulations were being performed within 10 km of the epicenter although one well was undergoing flowback

at the time of the M 5.0. While we cannot exclude these operations from having any influence on the occurrence of the M 5.0, they are unlikely to be the primary cause of the observed seismicity.

As hydrocarbon production is spatiotemporally related to WD activities, it is difficult to isolate the individual contributions of each type of operation. However, previous conservative stress estimates between 2007-2017 in the Delaware Basin found production to have resulted in a ~0.5 kPa hydrostatic pressure change (Skoumal et al., 2020), much smaller than the changes associated with atmospheric pressure loading or solid earth tides measured in deep disposal reservoirs (e.g., Barbour et al., 2019). The only other industrial operation that we are aware of that could explain the seismicity is WD.

The rates of injected fluid in the Delaware Basin are comparable to peak disposal rates during ~2014-2016 in the seismogenic areas of Oklahoma (Figure 10). While there are many other factors beyond injected volume that influence the hazard of induced seismicity that must be taken into account, this provides a relative understanding of the scale of operations in the Delaware Basin and the challenge of finding an economic solution to the issue.

In the Delaware Basin, most WD wells inject into the shallower Delaware Mountain Group while a smaller number of wells inject into the deeper Devonian, Silurian, and Ordovician rocks. Beneath the Delaware Mountain Group are multiple shale formations that are commonly targeted for unconventional hydrocarbon development. The tight association between these injection data and seismicity rates suggests that the major mapped fault immediately to the northeast of the M5 sequence (Figure 2a) is a barrier to horizontal flow, which could help explain the spatial distribution of induced earthquakes in the region. There is also the possibility for the interbedded shale formations to restrict vertical flow of shallower WD, potentially helping to insulate deeper fault structures from shallow injectors. Near the M 5.0 sequence, the majority of wells are injecting into the Delaware Mountain Group at ~1-2 km deep (Figure 3). Only two WD wells in our selected area injected into the deeper Silurian at depths of ~4.8 km. However, the two Silurian injectors are both high-rate wells, and one of these Silurian wells exceeded 2 million BBLs/month. Of the ~32,000 WD wells active since 2007 in Texas, only 15 wells in the entire state have had a larger monthly injection rate. These Silurian injection wells are within 1 km of the Precambrian basement (~5.5 km depth) (Ruppel et al., 2008). While the proximity of injection to a critically stressed fault is the primary factor controlling the likelihood of injection-induced seismicity (Skoumal et al., 2018), WD wells with similar, high-rate injection have been found to have increased associations with induced earthquakes (e.g., Scanlon et al., 2019).

Deeper, mature faults in crystalline rock that are induced to slip have been suggested to be associated with greater increases in hazard than faults within sedimentary strata (Kozłowska et al., 2018). Injecting fluids in proximity to the Precambrian basement increases the likelihood of induced seismicity (Skoumal et al., 2018) and was found to be the primary factor controlling induced seismicity in Oklahoma (Hincks et al., 2018). Based on surface deformation modeling, we find that slip during the M 5 mainshock was concentrated primarily at shallow depths, which suggests that the host fault may have breached the disposal formation. Similar findings of basement faults intersecting disposal formations have been documented in Oklahoma (Barnhart, et al. 2018; Kolawole, et al., 2019) and NE Texas (Magnani, et al., 2017). Future work could determine the role that both the shallow and deep injectors have on the stability of such faults in the Delaware Basin, as they likely represent an important component in designing an effective strategy for seismic hazard mitigation. In Oklahoma, seismicity rates declined following reductions in disposal volumes and shifting disposal from the basal Arbuckle to shallower

formations (Langenbruch & Zoback, 2016; Norbeck & Rubinstein, 2018; Dempsey & Riffault, 2019); similar efforts in the Delaware Basin might have a similar efficacy.

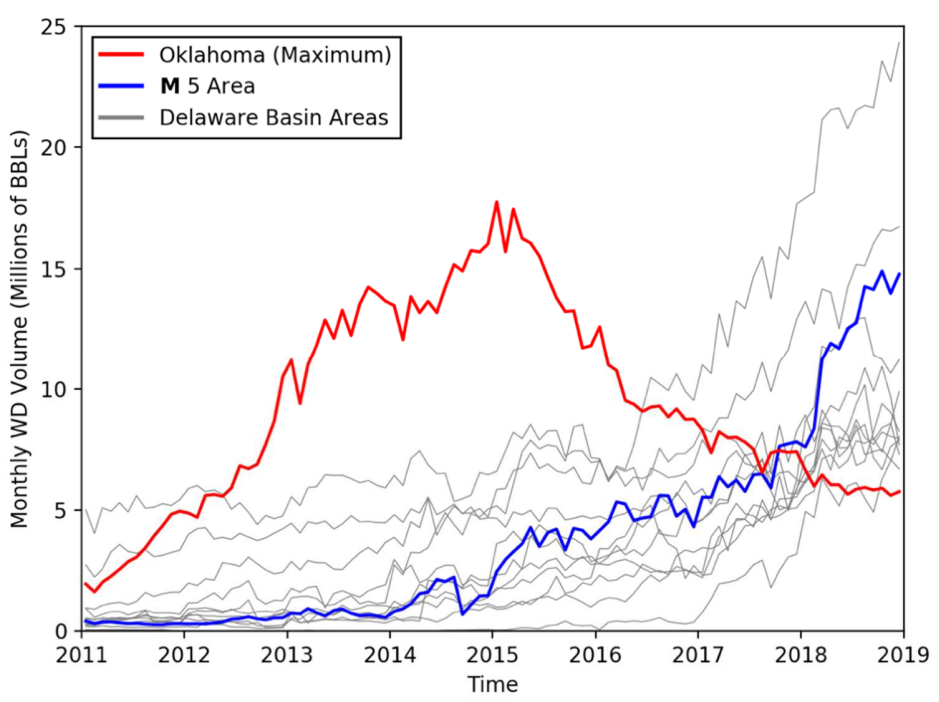


**Figure 10**. Monthly injected volumes for 30x30 km regions in the Delaware Basin compared against the 30x30 km region with largest injection volume located in Northern/Central Oklahoma. Only areas in the Delaware Basin with >5 million BBLs/month of disposal volume are shown.

### 4. Conclusions

Our earthquake catalog of 3,940 earthquakes indicate events in the area around the **M** 5.0 earthquake began several years prior to the mainshock. Our relocated catalog is consistent with a ENE ( $\sim$ 082°) normal fault dipping  $\sim$ 37° towards the south. Using InSAR-derived surface deformation, we invert for the kinematics of the **M** 5.0 rupture and conclude that the slip, and possibly the hypocenter, of the mainshock earthquake occurred at depths < 6 km. This relatively shallow depth is consistent with the depths of nearby WD wells, which are located at depths < 5 km. Our forecasts for the area around the **M** 5.0 indicate seismicity rates will likely continue to increase in the future, and similar scenarios may apply elsewhere in the Delaware Basin. The rates of injected fluid in regions of the Basin are comparable to peak disposal rates in Oklahoma during  $\sim$ 2014-2016 that led to widespread seismicity. If industry operations in the Delaware Basin continue unaltered, it is possible that additional **M**  $\geq$  5.0 earthquakes may be induced in the future. Understanding the mechanisms and operations responsible for the seismicity at a higher level of granularity will aid in mitigating this future seismic risk; however, the current coverage of seismometers on a local scale is sparse throughout much of the Delaware Basin, which limits the reliability of routinely determined earthquake locations and depths.

# Acknowledgments

All seismic data were obtained through the Incorporated Research Institutions for Seismology Data Management Center (https://iris.edu/hq/). Earthquake catalogs were obtained from the ANSS (https://earthquake.usgs.gov/data) and TexNet

from the ANSS (https://earthquake.usgs.gov/data) and TexNet (http://coastal.beg.utexas.edu/texnetcatalog). Sentinel 1 radar data were accessed through ESA's Copernicus Open Access Hub (https://scihub.compernicus.eu) and the Alaska Satellite Facility's Vertex site (https://search.asf.alaska.edu). Well data were retrieved from FracFocus (https://fracfocus.org), the Oklahoma Corporation Commission (http://www.occeweb.com), and the Texas Railroad Commission (https://rrc.texas.gov). All links were last accessed May 2020. Keith Knudsen, Sarah Minson, and Fred Pollitz provided constructive peer reviews that improved the manuscript. Updated operational data in Texas was provided by the Texas Railroad Commission, and we thank Sean Avitt, Jim Moore, and Aaron Velasco for their assistance.

The authors declare that they have no competing interests. Any use of trade, firm, or product names is for descriptive purposes only and does not imply endorsement by the U.S. Government.

## References

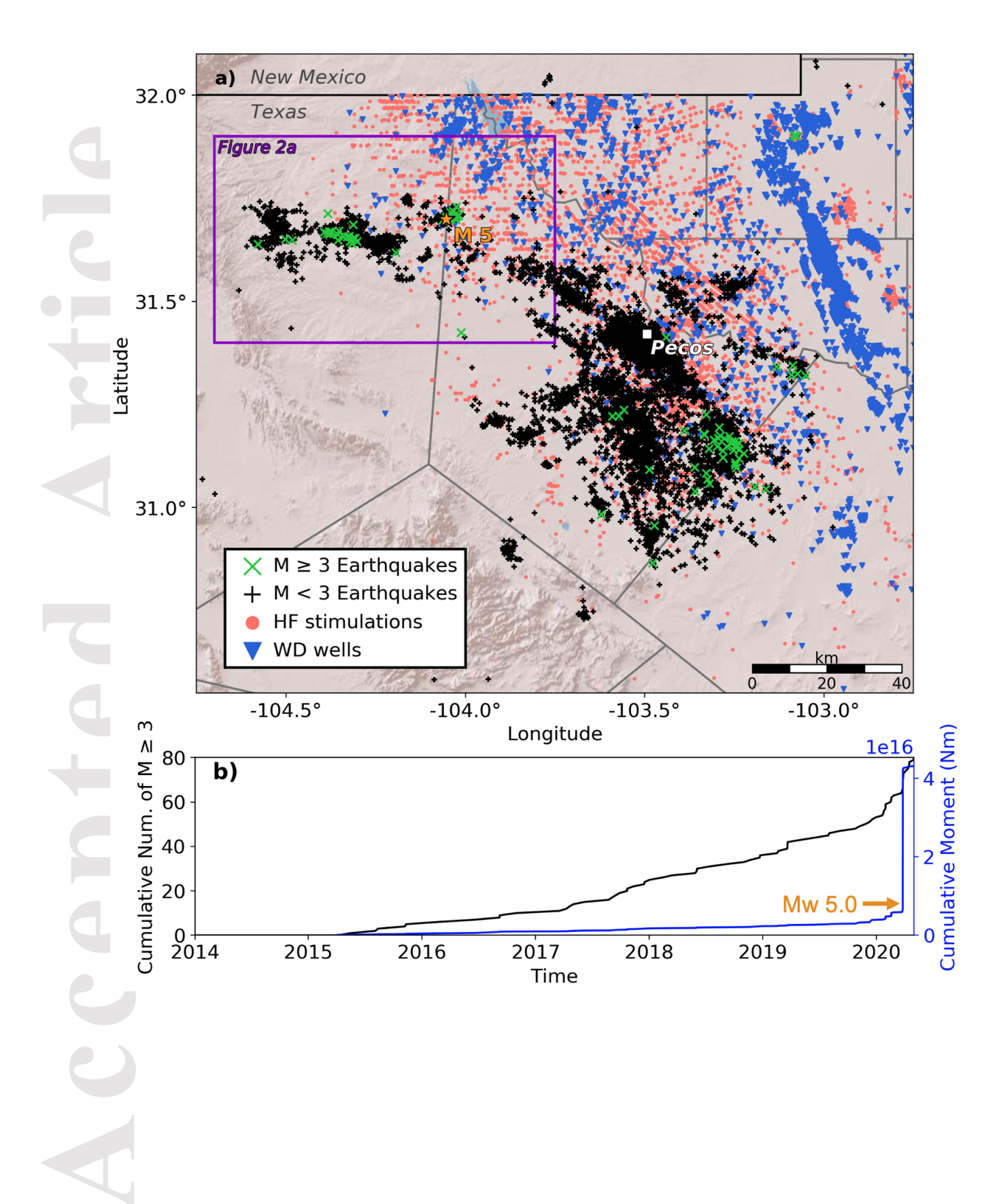
- Anderson, J. G. (1986). Seismic strain rates in the central and eastern United States, Bull. Seismol. Soc. Am. 76, no. 1, 273–290.
- Barbour, A. J., Norbeck, J. H., & Rubinstein, J. L. (2017), The effects of varying injection rates in Osage County, Oklahoma, on the 2016 Mw 5.8 Pawnee earthquake. Seismol Res Lett, 88(5): 1040–1053.
- Barbour, A. J., Xue, L., Roeloffs, E., & Rubinstein, J. L. (2019). Leakage and increasing fluid pressure detected in Oklahoma's wastewater disposal reservoir. Journal of Geophysical Research: Solid Earth: Solid Earth, 124, 2896–2919. doi: 10.1029/2019JB017327
- Barnhart, W. D., Yeck, W. L., & McNamara, D. E. (2018), Induced earthquake and liquefaction hazards in Oklahoma, USA: Constraints from InSAR, Remote Sensing of Environment, 218, 1-12, doi: 10.1016/j.rse.2018.09.005
- Blanpied, M. L., Marone, C. J., Lockner, D. A., Byerlee, J. D., and King, D. P. (1998), Quantitative measure of the variation in fault rheology due to fluid □rock interactions, J. Geophys. Res., 103(B5), 9691–9712, doi: 10.1029/98JB00162
- Byrd, R. H., Lu, P., Nocedal, J. and Zhu, C. (1995), A limited memory algorithm for bound constrained optimization, SIAM Journal on Scientific Computing, 16, 1190-1208, doi: 10.1137/0916069
- Calais, E., Han, J. Y., DeMets, C., & Nocquet, J. M. (2006). Deformation of the North American plate interior from a decade of continuous GPS measurements, J. Geophys. Res. 111, no. B6402, doi: 10.1029/2005JB004253
- Cochran, E. S., Skoumal, R. J., McPhillips, D., Ross, Z. E., & Keranen, K. M. (2020), Activation of optimally and unfavourably oriented faults in a uniform local stress field during the 2011 Prague, Oklahoma, sequence. Geophysical Journal International, 222(1), 153-168. doi: 10.1093/gji/ggaa153
- Davis, S. D., & Pennington, W. D. (1989). Induced seismic deformation in the Cogdell oil field of west Texas, Bull. Seismol. Soc. Am. 79, 1477–1495.
- Dempsey, D., & Riffault, J. (2019), Response of induced seismicity to injection rate reduction: Models of delay, decay, quiescence, recovery, and Oklahoma. Water Resources Research, 55(1), 656-681.

- Dieterich, J. (1994), A constitutive law for rate of earthquake production and its application to earthquake clustering, J. Geophys. Res., 99(B2), 2601–2618, doi: 10.1029/93JB02581
- Fan, Z., Eichhubl, P., & Newell, P. (2019), Basement fault reactivation by fluid injection into sedimentary reservoirs: Poroelastic effects. Journal of Geophysical Research: Solid Earth, 124, 7354–7369. doi: 10.1029/2018JB017062
- Farr, T. G., Rosen, P. A., Caro, E., Crippen, R., Duren, R., Hensley, S., et al. (2007). The Shuttle Radar Topography Mission. *Reviews of Geophysics*, 45, RG2004. doi: 10.1029/2005RG000183.
- Fasola, S. L., Brudzinski, M. R., Skoumal, R. J., Langenkamp, T., Currie, B. S., & Smart, K. J. (2019), Hydraulic Fracture Injection Strategy Influences the Probability of Earthquakes in the Eagle Ford Shale Play of South Texas. Geophysical Research Letters, 46(22), 12958-12967. doi: 10.1029/2019GL085167
- Frohlich, C., Hayward, C., Rosenblit, J. Aiken, C., Hennings, P., Savvaidis, A., Lemons, C., Horne, E., Walker, J. I., & DeShon, H. R. (2019), Onset and cause of increased seismic activity near Pecos, West Texas, USA from observations at the Lajitas TXAR Seismic Array. Journal of Geophysical Research: Solid Earth: Solid Earth. doi: 10.1029/2019JB017737
- Frohlich, C., & Davis, S. D. (2002), Texas Earthquakes, Univ. Texas Press, Austin, Texas, 275 pp.
- Funning, G.J., Parsons, B., Wright, T.J., (2005), Surface displacements and source parameters of the 2003 Bam (Iran) earthquake from Envisat advanced synthetic aperture radar imagery, J. geophys. Res., 110, B09406. doi: 10.1029/2004JB003338.
- Gan, W., & Frohlich, C. (2013), Gas injection may have triggered earthquakes in the Cogdell oil field, Texas, Proc. Natl. Acad. Sci. 110, no. 47, 18,786–18,791. doi: 10.1073/pnas.1311316110.
- Goebel, T. H. W., Weingarten, M., Chen, X., Haffener, J., and Brodsky, E. E. (2017). The 2016 Mw5.1 Fairview, Oklahoma earthquakes: Evidence for long-range poroelastic triggering at >40 km from fluid disposal wells. Earth and Planetary Science Letters, 472, 50-61
- Hincks, T., Aspinall, W., Cooke, R., & Gernon, T. (2018), Oklahoma's induced seismicity strongly linked to wastewater injection depth, Science 359, 1251–1255.
- Husen, S., and R. B. Smith (2004). Probabilistic earthquake relocation in three-dimensional velocity models for the Yellowstone National Park region, Wyoming, Bull. Seismol. Soc. Am. 94, no. 3, 880–896.
- Jónsson, S., Zebker, H., Segall, P., & Amelung, F. (2002). Fault slip distribution of the 1999 Mw 7.1 Hector Mine, California, earthquake, estimated from satellite radar and GPS measurements. Bulletin of the Seismological Society of America, 92, 1377–1389, doi: 10.1785/0120000922.
- Keranen, K. M., Savage, H. M., Abers, G.A., & Cochran, E. S. (2013), Potentially induced earthquakes in Oklahoma, USA: links between wastewater injection and the 2011 mw 5.7 earthquake sequence. Geology, 41(6):699–702.
- Keranen, K. M., & Weingarten, M. (2018). Induced seismicity. *Annual Review of Earth and Planetary Sciences*, 46:1, 149-174.
- Kolawole, F., C. S. Johnston, C. B. Morgan, J. C. Chang, K. J. Marfurt, D. A. Lockner, Z. Reches & B. M. Carpenter (2019), The susceptibility of Oklahoma's basement to seismic reactivation, Nat. Geosci., 12, 839–844, doi: 10.1038/s41561-019-0440-5

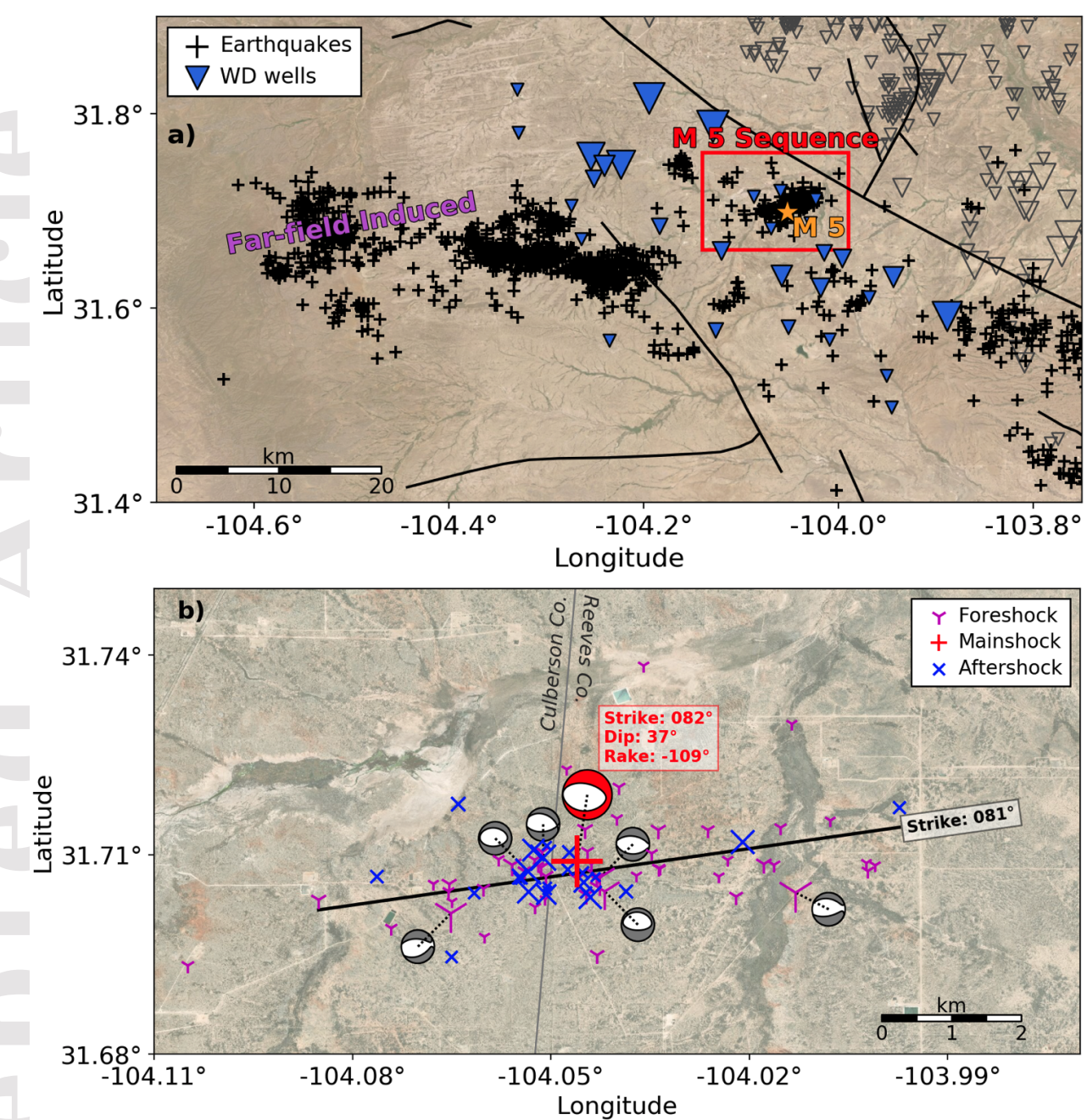
- Kozłowska, M., Brudzinski, M. R., Friberg, P., Skoumal, R. J., Baxter, N. D., & Currie, B. S. (2018), Maturity of nearby faults influences seismic hazard from hydraulic fracturing. Proceedings of the National Academy of Sciences, 115(8), E1720-E1729.
- Langenbruch, C., Weingarten, M., & Zoback, M. D. (2018), Physics-based forecasting of manmade earthquake hazards in Oklahoma and Kansas. Nature Communications, 9(1), 1-10.
- Langenbruch, C., & Zoback, M. D. (2016), How will induced seismicity in Oklahoma respond to decreased saltwater injection rates?. Science advances, 2(11), e1601542.
- Lockner, D. A. (1998), A generalized law for brittle deformation of Westerly granite, J. Geophys. Res., 103(B3), 5107–5123, doi: 10.1029/97JB03211
- Lohman, R. B., & Simons, M. (2005), Some thoughts on the use of InSAR data to constrain models of surface deformation: Noise structure and data downsampling. Geochemistry Geophysics Geosystems, 6, Q01007, doi: 10.1029/2004GC000841.
- Lomax, A., Virieux, J., Volant, P., & Berge-Thierry, C. (2000), Probabilistic earthquake location in 3D and layered models, in Advances in Seismic Event Location, Springer, Dordrecht, The Netherlands, 101–134.
- Lund Snee, J.-E., & Zoback, M. D. (2016), State of stress in Texas: Implications for induced seismicity, Geophys. Res. Lett., 43, 10,208-10,214, doi: 10.1002/2016GL070974
- Magnani, M. B., Blanpied, M. L., DeShon, H. R., & Hornbach, M. J. (2017), Discriminating between natural versus induced seismicity from long-term deformation history of intraplate faults, Science Advances, 3(11), e1701593, doi: 10.1126/sciadv.1701593
- Marone, C. (1998). The effect of loading rate on static friction and the rate of fault healing during the earthquake cycle. Nature, 391, 69–72, doi: 10.1038/34157
- McGarr, A., and Gay, N. C. (1978). State of stress in the Earth's crust. Annual Review of Earth and Planetary Sciences, 6(1), 405-436.
- McNamara, D. E., Hayes, G. P., Benz, H. M., Williams, R. A., McMahon, N. D., Aster, R. C., Holand, A., Sickbert, T., Herrmann, R., Briggs, R., Smoczyk, G., Bergman, E., & Earle, P. (2015), Reactivated faulting near Cushing, Oklahoma: increased potential for a triggered earthquake in an area of United States strategic infrastructure. Geophys Res Lett, 42(20):8328–8332
- Murray, J., & Langbein, J. (2006). Slip on the San Andreas fault at Parkfield, California, over two earthquake cycles, and the implications for seismic hazard. Bulletin of the Seismological Society of America, 96(4B), S283-S303.
- Norbeck, J. H., & Rubinstein, J. L. (2018), Hydromechanical earthquake nucleation model forecasts onset, peak, and falling rates of induced seismicity in Oklahoma and Kansas. Geophysical Research Letters, 45(7), 2963-2975.
- Ogwari, P. O., DeShon, H. R., & Hornbach, M. J. (2018). The Dallas- Fort Worth Airport earthquake sequence: Seismicity beyond injection period, Journal of Geophysical Research: Solid Earth, 123, 553–563, doi: 10.1002/2017JB015003.
- Pedersen, R., Jonsson, S., Arnadottir, T., Sigmundsson, F., and Feigl, K. L., (2003) Fault slip distribution of two June 2000 Mw6.5 earthquakes in South Iceland estimated from joint inversion of InSAR and GPS measurements, Earth Planet. Sci. Lett., 213, 487-502.
- Pennington, W. D., Davis, S. D., Carlson, S. M., Dupree, J., & Ewing, T. E. (1986), The evolution of seismic barriers and asperities caused by the depressuring of fault planes in oil and gas fields of south Texas, Bull. Seismol. Soc. Am. 76, 939–948.
- Rathje, E., P. Hennings, A. Savvaidis, & M. Young (2018). 2018 biennial report on seismic monitoring and research in Texas. https://www.beg.utexas.edu/texnet-cisr/reports

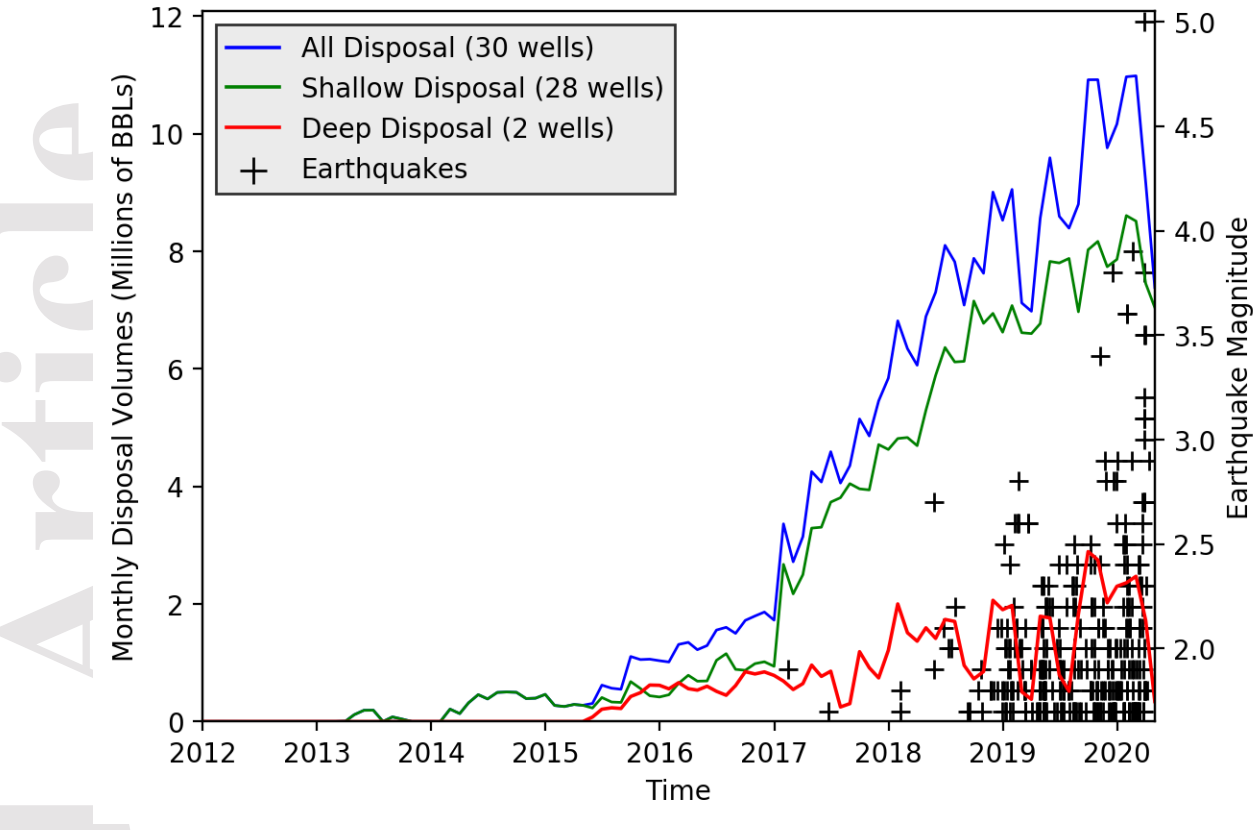
- Ruppel, S. C., Loucks, R. Kerans, C., Jones, R. H. Nance, H. S., Breton, C. L, et al. (2008). Integrated synthesis of the Permian Basin. http://www.beg.utexas.edu/resprog/permianbasin/integsynthesis.htm
- Ruppel, S.C., Jones, R.H., Breton, C.L. and Kane, J.A. (2005), Preparation of maps depicting geothermal gradient and Precambrian structure in the Permian basin. Contract report to the US Geological Survey Order, 04CRSA0834
- Savvaidis, A., Young, B., Huang, G. C. D., & Lomax, A. (2019), TexNet: A statewide seismological network in Texas. Seismological Research Letters. doi: 10.1785/0220180350
- Scanlon, B. R., Weingarten, M. B., Murray, K. E., & Reedy, R. C. (2019). Managing basin-scale fluid budgets to reduce injection-induced seismicity from the recent US shale oil revolution. Seismological Research Letters, 90(1), 171-182.
- Schaff, D. P., & Richards, P. G. (2014), Improvements in magnitude precision, using the statistics of relative amplitudes measured by cross correlation. Geophysical Journal International, 197(1), 335–350. doi: 10.1093/gji/ggt433
- Schultz, R., & Wang, R. (2020). Newly emerging cases of hydraulic fracturing induced seismicity in the Duvernay East Shale Basin. Tectonophysics. doi: 10.1016/j.tecto.2020.228393
- Segall, P., & Lu, S. (2015). Injection-induced seismicity: Poroelastic and earthquake nucleation effects. Journal of Geophysical Research: Solid Earth, 120, 5082–5103, doi: 10.1002/2015JB012060
- Shapiro, S. A., & Dinske, C. (2009). Fluid ☐ induced seismicity: Pressure diffusion and hydraulic fracturing. Geophysical Prospecting, 57(2), 301-310.
- Skoumal, R. J., Barbour, A. J., Brudzinski, M. R., Langenkamp, T., & Kaven, J. O. (2020), Induced Seismicity in the Delaware Basin, Texas. Journal of Geophysical Research: Solid Earth, 125(1), e2019JB018558.
- Skoumal, R. J., Brudzinski, M. R., & Currie, B. S. (2018), Proximity of Precambrian basement affects the likelihood of induced seismicity in the Appalachian, Illinois, and Williston Basins, central and eastern United States. Geosphere, 14(3), 1365-1379.
- Skoumal, R. J., Ries, R., Brudzinski, M. R., Barbour, A. J., & Currie, B. S. (2018). Earthquakes induced by hydraulic fracturing are pervasive in Oklahoma. Journal of Geophysical Research: Solid Earth, 123(12), 10-918.
- Skoumal, R. J., Brudzinski, M. R., Burrie, B. S., Levy, J. (2014). Optimizing multi-station earthquake template matching through re-examination of the Youngstown, Ohio, sequence. Earth Planet. Sci. Let., 405. doi: 10.1016/j.epsl.2014.08.033
- Skoumal, R. J., Kaven, J. O., & Walter, J. I. (2019), Characterizing seismogenic fault structures in Oklahoma using a relocated template ☐matched catalog. Seismological Research Letters, 90(4), 1535-1543. doi: 10.1785/0220190045
- Trugman, D. T., & Shearer, P. M. (2017), GrowClust: A hierarchical clustering algorithm for relative earthquake relocation, with application to the Spanish Springs and Sheldon, Nevada, earthquake sequences, Seismol. Res. Lett. 88, no. 2A, 379–391, doi: 10.1785/0220160188.
- Wahba, G. (1990), Spline models for observational data, in CBMS \(\subseteq\) NSF Regional Conference Series in Applied Mathematics, vol. 59, edited by J. Ward and E. Cheney, p. 169, SIAM: Society for Industrial and Applied Mathematics, Philadelphia, Pa.

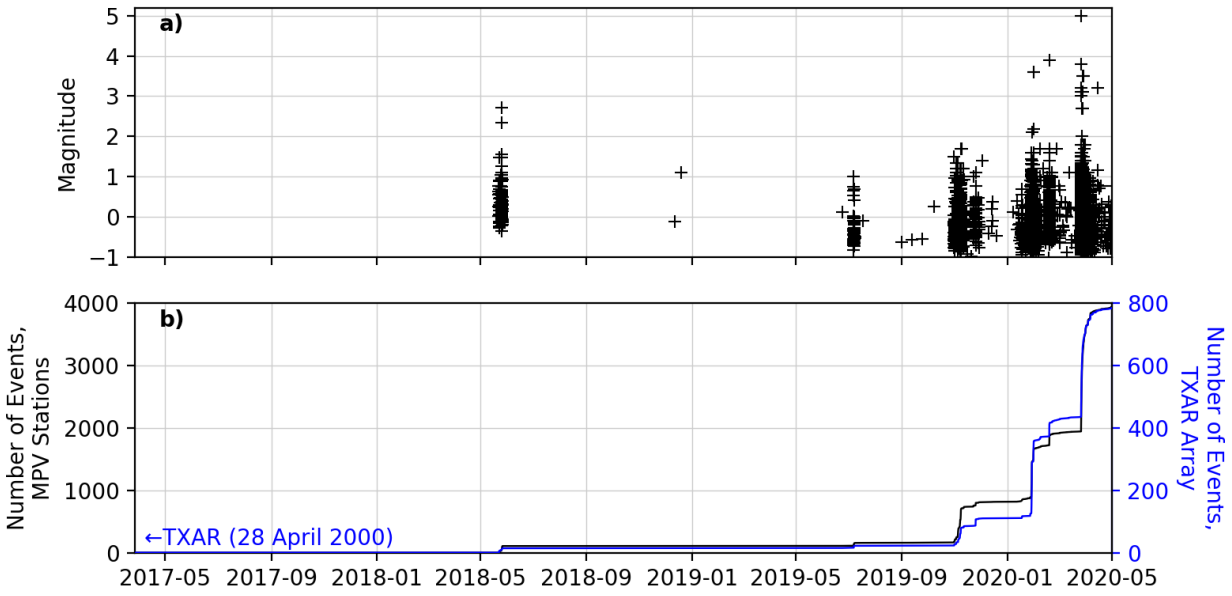
- Wang, H. F. (2000). Theory of Linear Poroelasticity with Applications to Geomechanics and Hydrogeology, Princeton Series in Geophysics, Princeton University Press, Princeton, New Jersey
- Wang, R., & Kümpel, H. J. (2003). Poroelasticity: Efficient modeling of strongly coupled, slow deformation processes in a multilayered half-space, Geophysics 68, no. 2, 705–717, doi: 10.1190/1.1567241
- Wicks, C., Weaver, C., Bodin, P. & Sherrod, B. (2013). InSAR evidence for an active shallow thrust fault beneath the city of Spokane Washington, USA. Journal of Geophysical Research, 118, 1-9. doi: 10.1002/jgrb.50118.
- Yeck W. L., Weingarten, M., Benz, H. M., McNamara, D. E., Bergman, E. A., Herrmann, R. B., Rubinstein, J. L., & Earle, P. S. (2016), Far-field pressurization likely caused one of the largest injection induced earthquakes by reactivating a large preexisting basement fault structure. Geophys Res Lett, 43(19):10–198
- Yeck, W. L., Hayes, G. P., McNamara, D. E., Rubinstein, J. L., Barnhart, W. D., Earle, P. S., & Benz, H. M. (2017), Oklahoma experiences largest earthquake during ongoing regional wastewater injection hazard mitigation efforts, Geophysical Research Letters, 44(2), 711-717, doi: 10.1002/2016GL071685
- Zhai, G., & Shirzaei, M. (2018). Fluid injection and time-dependent seismic hazard in the Barnett Shale, Texas. Geophysical Research Letters, 45, 4743–4753, doi: 10.1029/2018GL077696
- Zhai, G., Shirzaei, M., Manga, M., & Chen, X. (2019). Pore-pressure diffusion, enhanced by poroelastic stresses, controls induced seismicity in Oklahoma. Proceedings of the National Academy of Sciences, 116(33), 16228-16233, doi: 10.1073/pnas.1819225116

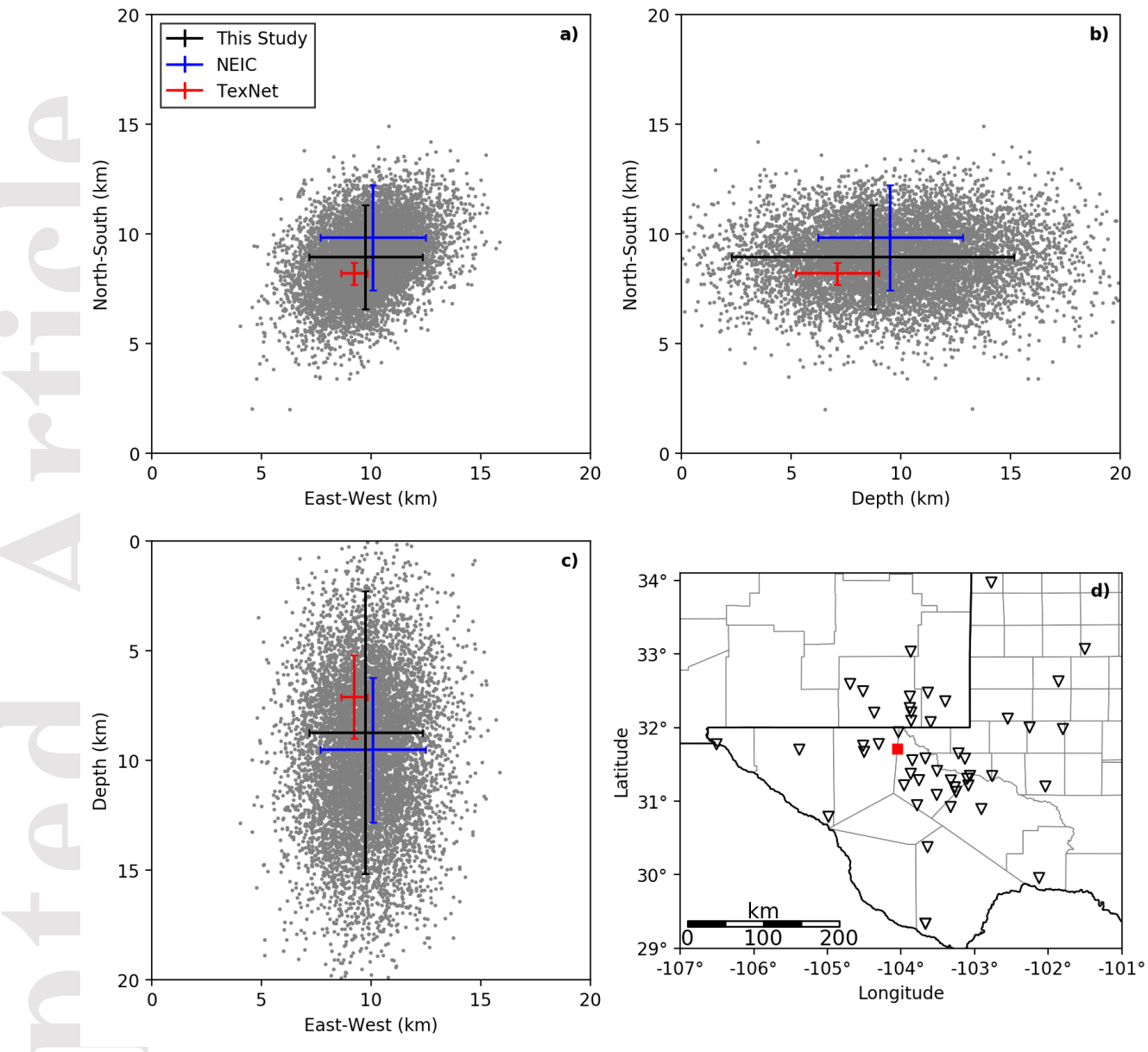












a) •

-104.2°

-104.1°

-104.0°

